Acta Pharmaceutica Sinica B 2022;12(12):4472–4485

Chinese Pharmaceutical Association
Institute of Materia Medica, Chinese Academy of Medical Sciences

Acta Pharmaceutica Sinica B

www.elsevier.com/locate/apsb
www.sciencedirect.com

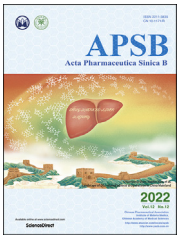

ORIGINAL ARTICLE

Biodegradable calcium sulfide-based nanomodulators for H_2S-boosted Ca^{2+}-involved synergistic cascade cancer therapy

Chuchu Lin[a], Chenyi Huang[a], Zhaoqing Shi[b], Meitong Ou[a], Shengjie Sun[a], Mian Yu[a], Ting Chen[b], Yunfei Yi[a], Xiaoyuan Ji[a,c], Feng Lv[b], Meiying Wu[a,*], Lin Mei[b,*]

[a]*School of Pharmaceutical Sciences (Shenzhen), Shenzhen Campus of Sun Yat-sen University, Shenzhen 518107, China*
[b]*Tianjin Key Laboratory of Biomedical Materials, Key Laboratory of Biomaterials and Nanotechnology for Cancer Immunotherapy, Institute of Biomedical Engineering, Chinese Academy of Medical Sciences and Peking Union Medical College, Tianjin 300192, China*
[c]*Academy of Medical Engineering and Translational Medicine, Medical College, Tianjin University, Tianjin 300072, China*

Received 10 May 2022; received in revised form 1 July 2022; accepted 18 July 2022

KEY WORDS

Calcium sulfide;
Hydrogen sulfide;
Calcium overload;
Oxidative stress;
Photothermal therapy;
Biodegradability;
Controllable release;
Nanomodulators

Abstract Hydrogen sulfide (H_2S) is the most recently discovered gasotransmitter molecule that activates multiple intracellular signaling pathways and exerts concentration-dependent antitumor effect by interfering with mitochondrial respiration and inhibiting cellular ATP generation. Inspired by the fact that H_2S can also serve as a promoter for intracellular Ca^{2+} influx, tumor-specific nanomodulators (I-CaS@PP) have been constructed by encapsulating calcium sulfide (CaS) and indocyanine green (ICG) into methoxy poly (ethylene glycol)-*b*-poly (lactide-*co*-glycolide) (PLGA-PEG). I-CaS@PP can achieve tumor-specific biodegradability with high biocompatibility and pH-responsive H_2S release. The released H_2S can effectively suppress the catalase (CAT) activity and synergize with released Ca^{2+} to facilitate abnormal Ca^{2+} retention in cells, thus leading to mitochondria destruction and amplification of oxidative stress. Mitochondrial dysfunction further contributes to blocking ATP synthesis and downregulating heat shock proteins (HSPs) expression, which is beneficial to overcome the heat endurance of tumor cells and strengthen ICG-induced photothermal performance. Such a H_2S-boosted Ca^{2+}-involved tumor-specific therapy exhibits highly effective tumor inhibition effect with almost complete elimination within 14-day treatment, indicating the great prospect of CaS-based nanomodulators as antitumor therapeutics.

*Corresponding author. Tel./fax: +18665387360.
E-mail addresses: wumy53@mail.sysu.edu.cn (Meiying Wu), meilin@bme.pumc.edu.cn (Lin Mei).

Peer review under the responsibility of Chinese Pharmaceutical Association and Institute of Materia Medica, Chinese Academy of Medical Sciences.

https://doi.org/10.1016/j.apsb.2022.08.008

1. Introduction

Hydrogen sulfide (H_2S) is a colorless gas with a distinctive odor like rotten eggs, which has been recognized as a biological gasotransmitter molecule alongside nitric oxide (NO) and carbon monoxide (CO). Since these gasotransmitters can easily diffuse across cell membranes, they participate in a wide range of cellular functions, and physiological and pathological processes[1−3]. Under normal physiological conditions, endogenous H_2S is produced through both enzymatic and nonenzymatic pathways that differ in various tissues and organs, playing an important role in maintaining homeostasis throughout the body[4,5]. Similar to NO and CO, low concentration (25−50 μmol/L) of H_2S generally exerts cytoprotective, anti-inflammatory, and antioxidant functions, such as regulating neuronal excitation, improving myocardial systolic and diastolic dysfunction, reducing infarcted myocardial injury or delaying atherosclerosis, etc[6−8]. However, a high concentration (>200 μmol/L) of H_2S can cause pro-oxidant and DNA-damaging effects[9]. Therefore, the ingenious use of H_2S in a certain concentration represents a promising therapeutic approach for disease treatment.

Cancer, characterized by the uncontrolled growth and proliferation of cells, has been considered as one of the most devastating diseases[10,11]. H_2S produced in excess has been shown to inhibit the activity of mitochondrial complex IV and block mitochondrial electron transport and adenosine triphosphate (ATP) synthesis[12,13]. In addition, this gas mediator can regulate enzyme activity and ion flow across ion channels on the plasma membrane[13−15]. For example, H_2S gas has been reported to effectively suppress the catalase (CAT) activity of tumor cells[16], or to facilitate the reduction of Fe^{3+} to Fe^{2+}[17], thus promoting the efficiency of chemodynamic therapy (CDT) by elevating intracellular H_2O_2 levels and disrupting redox homeostasis[18]. More interestingly, H_2S can also open ATP-sensitive potassium channels and activate voltage-dependent potassium channels and L-shaped calcium channels, leading to membrane potential depolarization and calcium influx[19]. Likewise, calcium ion (Ca^{2+}) is a versatile intracellular messenger that controls multiple cellular activities and functions[20]. Recent studies have uncovered that excessive Ca^{2+} retention in cells can induce increased ROS production by causing mitochondrial dysfunction and oxidative stress elevation, and ultimately disturb cellular metabolism and induce intrinsic cell apoptosis[21]. Encouragingly, H_2S-boosted Ca^{2+}-involved tumor-specific therapy will become a novel method for innovative therapeutic intervention, but has been rarely studied.

Herein, we proposed a facile high-temperature co-precipitation method to construct calcium sulfide (CaS)-based nanomodulators (I-CaS@PP) for H_2S-boosted Ca^{2+}-involved tumor-specific therapy, wherein both CaS and indocyanine green (ICG) were stabilized by methoxy poly (ethylene glycol)-*b*-poly (lactide-*co*-glycolide) (PLGA-PEG) that could not only ensure high biocompatibility but also improve the stability of CaS in the physiological environment (Fig. 1). The obtained I-CaS@PP achieved superior biodegradability and controllable release of Ca^{2+} and H_2S in the acidic tumor microenvironment as in Eqs. (1) and (2):

$$CaS + 2H_2O \rightarrow Ca(OH)_2 + H_2S \quad (1)$$

$$Ca(OH)_2 + 2H^+ \rightarrow Ca^{2+} + 2H_2O \quad (2)$$

Specifically, the generated H_2S could not only inhibit the activity of CAT, leading to the increase of intracellular H_2O_2 concentration and the enhancement of oxidative stress, but also could promote Ca^{2+} influx and synergistically the generated Ca^{2+} to trigger Ca^{2+} overload. Meanwhile, the excessive Ca^{2+} retention in tumor cells led to mitochondrial dysfunction with concomitant inhibition of ATP synthesis, thus downregulating the expression of heat shock proteins (HSPs) that depend on ATP energy supply[22], and reversing the tumor resistance to thermal energy, resulting in synergistically enhancing photothermal treatment (PTT) effect of ICG[23,24]. Overall, this study presented a novel CaS-based nanomodulator with remarkable tumor heat resistance suppression to achieve synergistic tumor treatment.

2. Materials and methods

2.1. Materials

$Ca(CH_3COO)_2 \cdot H_2O$ (99.9%) was purchased from Aladdin (Shanghai, China). Oleic acid (OA), oleylamine (OAm), trioctylamine (TOA), *N*,*N*′-diphenylthiourea (DPTU) and indocyanine green (ICG) were obtained from Sigma−Aldrich Co., Ltd. (Beijing, China). Poly (lactide-*co*-glycolide)-block-poly (ethylene glycol) (PLGA-PEG) was purchased from Xi'an Ruixi Biotech Biochemistry Technology Co., Ltd. (Xi'an, China). H_2S content detection Kit was purchased from Beijing Solarbio Science & Technology Co., Ltd. (Beijing, China). Fetal bovine serum (FBS) was obtained from Newzerum Ltd. (Christchurch, New Zealand). Cell Counting Kit-8 (CCK-8) was obtained from APExBIO Technology LLC. (Houston, TX, USA). WSP-1 was obtained from AAT Bioquest (Sunnyvale, CA, USA). Calcium Colorimetric Assay Kit, 4′,6-diamidino-2-phenylindole (DAPI), Fluo-4 AM, Live/Dead Calcein Acetoxymethyl Ester (Calcein-AM)/Propidium Iodide (PI) Double Staining Kit, Annexin V-FITC/PI Apoptosis Detection Kit, MitoTracker® Green FM, Hochest 33342, Bicinchoninic Acid (BCA) Kit, ATP Assay Kit, Reactive Oxygen Species Assay Kit, JC-1 Kit, Hematoxylin & Eosin (H&E) Staining Kit, TdT-mediated dUTP Nick-End Labeling (TUNEL) Apoptosis Assay Kit were purchased from Beyotime Institute of Biotechnology (Shanghai, China). Paraformaldehyde solution was obtained from Yongjin Biotechnology Co., Ltd. (Guangzhou, China). Anti-HSP-70 antibody and anti-HSP-90 antibody were obtained from Abcam Inc. (ab2787, ab13492, Cambridge, MA, USA). All chemical reagents were of analytical grade and used as received without further purification unless otherwise stated. Deionized water (Millipore) was used to prepare the required aqueous solution.

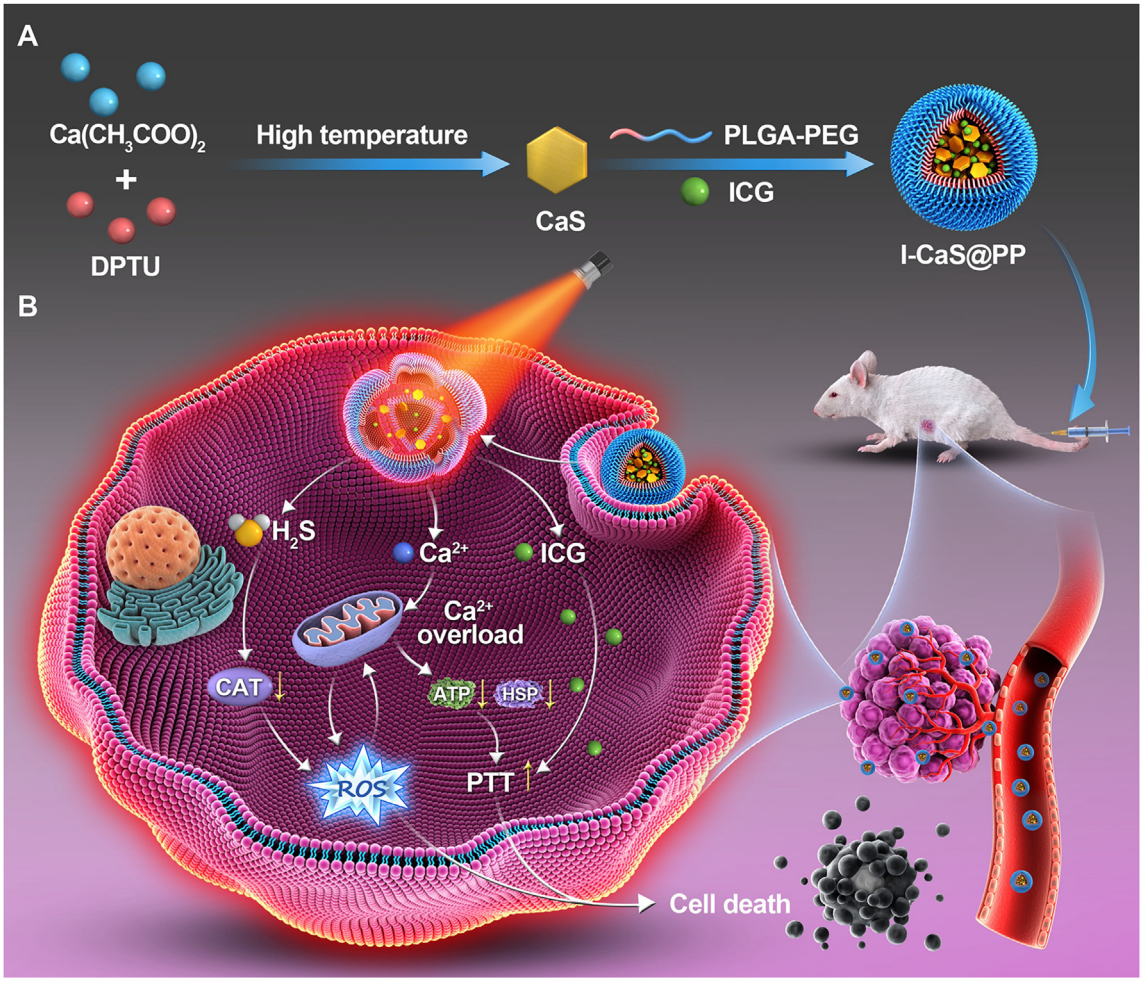

Figure 1 Schematic illustration of (A) the preparation of I-CaS@PP and (B) the mechanism of H_2S-boosted Ca^{2+}-involved tumor-specific therapy.

2.2. *Synthesis of CaS*

CaS nanoparticles (NPs) were synthesized through a high-temperature co-precipitation[25]. Briefly, 0.9993 mmol/L of $Ca(CH_3COO)_2 \cdot H_2O$ were mixed with 2 mL of OA, 12 mL of OAm and 6 mL of TOA in a 50 mL three-necked round-bottom flask. The resulting mixture was heated to 120 °C under an argon (Ar) flow with constant stirring for 30 min to remove the residual water and oxygen, and then heated to 160 °C and stirred for another 30 min to form a clear solution. After cooling down to room temperature (RT), 10 mL of ethanol solution containing 3 mmol/L of DPTU was added and the solution was stirred at 80 °C for 30 min to remove ethanol. After ethanol was evaporated, the resulting solution was heated to 320 °C under an Ar flow with vigorous stirring for 60 min, and then cooled down to RT. The obtained NPs were precipitated by addition of 30 mL of ethanol, collected by centrifugation, washed with ethanol thrice, and finally redispersed in cyclohexane or tetrahydrofuran.

2.3. *Synthesis of I-CaS@PP*

First, 10 mg of CaS, 10 mg of ICG and 50 mg of PLGA-PEG were dissolved in 1 mL of tetrahydrofuran, and the obtained solution was sonicated for 5 min. Then, the whole obtained solution was injected into 4 mL of water under vigorous stirring for 5 min at RT. The obtained solution was centrifuged at 20,000 rpm (Hunan Xiangyi Laboratory Instrument Development Co., Ltd., GL-21M, Changsha, China) for 20 min and this step was repeated thrice. The precipitate was separated to obtain I-CaS@PP. The supernatant was isolated and used to determine the ICG encapsulation efficiency. The concentration of unencapsulated ICG in the supernatant was measured using an ultraviolet spectrophotometer (PerkinElmer, LAMBDA 365, Waltham, MA, USA). CaS@PPs were prepared by a similar process as above but without the addition of ICG.

2.4. *Characterization*

Transmission electron microscopy (TEM) images were acquired on a JEM-2100UHR microscope (JEOL, JEM-2100UHR, Tokyo, Japan). X-ray photoelectron spectroscopy (XPS, Thermo Fisher Scientific Inc., ESCALAB 250Xi, Asheville, NC, USA) and energy dispersive spectrometer (EDS) were applied to analyze the chemical constitutions of CaS, CaS@PP and I-CaS@PP. X-ray diffraction (XRD, Bruker, Bruker D8, Karlsruhe, Germany) was performed to analyze the crystal structure of CaS and I-CaS@PP. The hydrodynamic particle sizes and zeta potentials of NPs were monitored by dynamic light scattering (DLS, Brookhaven

Instruments Corporation, NanoBrook 90 Plus PALS, New York, NY, USA). The loading amount of ICG in I-CaS@PP was determined based on the UV−Vis absorbance peak at 780 nm, and it was calculated according to the followed Eq. (3):

$$\text{The loading amount of ICG (\%)} = (\text{Amount of ICG in feed} - \text{Amount of ICG in the supernatant})/(\text{Amount of I-CaS@PP}) \times 100 \quad (3)$$

The loading amount of CaS in I-CaS@PP was determined by detecting Ca and S amounts in I-CaS@PP using ICP-MS (Thermo Fisher Scientific Inc., Thermo ICAP PRO, NC, USA).

2.5. *In vitro degradation of I-CaS@PP*

To determine the degradation of I-CaS@PP, 1 mg of I-CaS@PP were dispersed into phosphate buffer solutions (PBS, 10 mL) with varied pH values (7.4, 6.5 or 5.5). The testing solutions were incubated in a water bath at 37 °C under gently shaking. A small amount of solution (100 μL) was taken out at the given time and centrifuged. The precipitate was redispersed in water and observed by TEM (JEOL).

2.6. *H_2S and Ca^{2+} release in vitro*

The pH-sensitive H_2S release was evaluated by adding I-CaS@PP to phosphate buffer solutions (1.5 mg/mL) with different pH values (7.4, 6.5 or 5.5) and gently shaking at 37 °C. And then, the supernatant was collected by centrifugation (20,000 rpm, 20 min) (Hunan Xiangyi Laboratory Instrument Development Co., Ltd., GL-21M) at 0.2, 0.5, 1, 2, 4, 8, 12, 24 and 48 h. The H_2S concentration was determined with the H_2S content detection kit. In addition, the group with different concentrations (3.0 and 4.5 mg/mL) and laser irradiation at pH 5.5 was also performed.

To investigate the effect of pH on Ca^{2+} release, I-CaS@PP were dispersed into buffer solutions (1.5 mg/mL) with different pH values (7.4, 6.5 or 5.5) and gently shaken at 37 °C. And then, the supernatants were collected by centrifugation (20,000 rpm, 20 min) (Hunan Xiangyi Laboratory Instrument Development Co., Ltd., GL-21M) at 0.2, 0.5, 1, 2, 4, 12, 24 and 48 h. The concentration of Ca^{2+} was determined by a calcium colorimetric assay kit. In addition, the group with laser irradiation at pH 5.5 was also performed.

2.7. *Photothermal effect of I-CaS@PP*

To systematically evaluate the photothermal performance of I-CaS@PP, the temperature changes of I-CaS@PP were assessed through exposing I-CaS@PP aqueous solutions with different concentrations (5, 10, 20, 30 and 40 μg/mL) to 808 NIR laser at different power densities (0.5, 1.0 and 1.2 W/cm^2) for 2 min and monitored with IR thermal camera (FLUKE, TI100 Infrared Camera FLK-TI100 9HZ, Everett, WA, USA). To compare the photothermal stability of I-CaS@PP and free ICG, I-CaS@PP and free ICG (at an equal ICG concentration of 50 μg/mL) were irradiated by an 808 nm laser at the same power densities of 1.2 W/cm^2 in five repeated cycles of 1 min irradiation ON and 5 min OFF. The photothermal conversion efficiency (η) of I-CaS@PP was monitored and calculated according to the previous reports[26−28].

2.8. *Cell culture*

The human breast cancer cells (4T1) cells were obtained from the American Type Culture Collection. 4T1 were cultured in high glucose Dulbecco's modified Eagle's medium (DMEM, Gibco, Waltham, MA, USA) supplemented with 10% FBS (Newzerum, New Zealand), 100 U/mL penicillin and 100 μg/mL streptomycin (Hyclone, Logan, UT, USA) at 37 °C and 5% CO_2 in a humidified incubator (Thermo Fisher Scientific Inc., Thermo 3111, Rochester, NY, USA).

2.9. *Cellular uptake*

To investigate the cellular internalization and mitochondria profile of I-CaS@PP, 4T1 cells were seeded in confocal dishes (5×10^4 cells per dish) and cultured at 37 °C for 24 h. After that, cells were treated with I-CaS@PP for different time points (1, 3, or 6 h). At the end of incubation, the redundant media were removed by washing with cold PBS three times followed by observation under a confocal laser scanning microscope (CLSM, Zeiss, LSN880, Jena, Germany). Furthermore, flow cytometry (Beckman coulter, CytoFLEX S, Indianapolis, IN, USA) was also used to quantitatively detect the cellular uptake, wherein 4T1 cells were treated as described above.

2.10. *In vitro cytotoxicity assay*

The *in vitro* cytotoxicity of nanoparticles against 4T1 cells was determined by the standard Cell Counting Kit-8 (CCK-8) assay. Briefly, 4T1 cells were cultured in 96-well plates at a density of 5.0×10^3 cells per well and incubated for 24 h. Then, cells were treated with different concentrations of ICG, CaS@PP and I-CaS@PP and continued to culture for 24 h. For the NIR irradiation group, cells were irradiated with 808 nm laser at 1.2 W/cm^2 for 2 min after incubation for 12 h. After washing with PBS, the typical CCK-8 Kit was used to determine the relative cell viabilities. The absorbance was measured at the wavelength of 450 nm.

The amounts of live/dead cells were further determined using a live/dead calcein-AM/PI double stain kit. Briefly, 4T1 cells were seeded in 6-well plates and cultured overnight. Afterward, the media were replaced by fresh DMEM media, ICG, CaS@PP and I-CaS@PP at an equal Ca^{2+} concentration of 20 μg/mL. After incubation for another 6 h, the laser-required cells were irradiated with an 808 nm laser at 1.2 W/cm^2 for 2 min and continued to culture for another 6 h. Finally, cells were stained with calcein-AM/PI solution for 20 min and observed by fluorescence microscope (Leica Microscope Ltd., Leica DMIRB, Wetzlal, Germany).

2.11. *Intracellular H_2S generation*

4T1 cells were seeded in confocal dishes (5×10^4 cells per dish) and cultured at 37 °C for 24 h. After that, the media were replaced by fresh DMEM media (control group), CaS@PP (CaS@PP group) and I-CaS@PP (I-CaS@PP group and I-CaS@PP + L group) (at an equal Ca^{2+} concentration of 20 μg/mL). After incubation for 4 h, the laser-required cells were irradiated with an 808 nm laser at 1.2 W/cm^2 for 2 min and continued to culture for another 2 h. After removing the residual nanoparticles and washing with cold PBS three times, WSP-1 was added and incubated for 30 min. Finally, cells were imaged using CLSM (Zeiss) and quantified by ImageJ software (NIH).

2.12. Intracellular Ca^{2+} concentration

4T1 cells were seeded in confocal dishes (5×10^4 cells per dish) and cultured for 24 h. Subsequently, cells were washed with PBS and treated with fresh DMEM media, $CaCl_2$, CaS@PP, I-CaS@PP, I-CaS@PP + EGTA, I-CaS@PP + L, I-CaS@PP + L + EGTA at an equal concentration of Ca^{2+} (20 μg/mL) for 12 h. The laser-required cells were irradiated with an 808 nm laser at 1.2 W/cm^2 for 2 min after treatment for 10 h, followed by incubation for another 2 h. Cells were then washed with PBS, and a Fluo-4 AM probe was utilized to stain intracellular Ca^{2+}, followed by observation under CLSM (Zeiss) and quantification with ImageJ software (NIH).

2.13. Detection of mitochondrial state

To observe the change of mitochondria state during drug uptake, cells were treated with I-CaS@PP for different time points (1, 2, 4, 6 and 12 h). At the end of incubation, the redundant media were removed, washed with cold PBS three times and stained with Mitotracker green and Hochest 33342, followed by observation under a confocal laser scanning microscope (CLSM, Zeiss).

2.14. Detection of mitochondrial membrane potential

Changes of mitochondrial membrane potential ($\Delta\psi_m$) were measured by using JC-1 fluorescent dye. Briefly, 4T1 cells were seeded in confocal dishes (5×10^4 cells per dish) and cultured overnight. Subsequently, cells were treated with fresh DMEM media (control group), 20 μg/mL of CaS@PP (CaS@PP group) and 20 μg/mL of I-CaS@PP (I-CaS@PP group and I-CaS@PP + L group) for 24 h. Cells in I-CaS@PP + L group were irradiated with an 808 nm laser at 1.2 W/cm^2 for 2 min after treatment for 12 h, followed by incubation for another 12 h. Then, cells were incubated with 500 μL of JC-1 dye for 20 min in the dark, washed with fresh DMEM media and observed under CLSM (Zeiss).

2.15. Measurement of intracellular ATP content

4T1 cells were seeded in 6-well plates and treated with fresh media (control group), CaS@PP (CaS@PP group) and I-CaS@PP (I-CaS@PP group and I-CaS@PP + L group) for 24 h. After incubation, cells were lysed, followed by centrifugation for 5 min at 12,000×*g* (Eppendorf, Eppendorf 5424R, Hamburg, Germany). The resulting supernatant was collected for measurement of intracellular ATP content according to the instruction of the ATP testing kit.

2.16. Measurement of intracellular catalase activity

To investigate the effect of H_2S generated from nanoparticles on intracellular catalase activity, 4T1 cells were seeded in 6-well plates and treated with fresh media (control group), CaS@PP (CaS@PP group) and I-CaS@PP (I-CaS@PP group and I-CaS@PP + L group) for 24 h. After incubation, cells were lysed followed by centrifugation for 5 min at 12,000×*g* (Eppendorf). The resulting supernatant was collected for measurement of intracellular catalase activity according to the instruction of the catalase assay Kit.

2.17. Detection of ROS production

Intracellular ROS production was determined by using 2′,7′ dichlorodihydrofluorescein diacetate (DCFH-DA). Briefly, 4T1 cells were seeded in 6-well plates and treated with fresh DMEM media (control group), $CaCl_2$, CaS@PP, I-CaS@PP, I-CaS@PP + EGTA, I-CaS@PP + L, I-CaS@PP + L + EGTA at an equal concentration of Ca^{2+} (20 μg/mL). After incubated for 12 h, the laser-required cells were irradiated with an 808 nm laser at 1.2 W/cm^2 for 2 min, followed by incubation for another 12 h. After 24 h incubation, 500 μL of DCFH-DA stock solution (20 μmol/L) was added to each well and incubated for 30 min at 37 °C in the dark. Finally, the images were acquired under CLSM (Zeiss). Furthermore, intracellular ROS production was also quantitatively determined by flow cytometry, wherein 4T1 cells were treated as described above.

2.18. Western blotting analysis of HSPs

Western blotting analysis was conducted to study the expressions of HSP-70 and HSP-90 in cells treated with fresh DMEM media (control group), fresh DMEM media + 40 °C, $CaCl_2$ + 40 °C, CaS@PP, I-CaS@PP, I-CaS@PP + L, I-CaS@PP + L + EGTA at an equal concentration of Ca^{2+} (20 μg/mL). For the groups treated with 40 °C, the cells were firstly incubated with fresh DMEM media or $CaCl_2$ for 12 h, and then cultured in an air-bath thermostat at 40 °C for 2 min. The cells were subsequently returned to the incubator for another 12 h. For NIR irradiating groups, after being treated with nanoparticles for 12 h, the cells were irradiated by an 808 nm laser at 1.2 W/cm^2 for 2 min and then incubated for another 12 h. After incubation, the cells were washed with PBS twice, followed by the addition of lysis buffer on ice. Subsequently, Western blotting analysis was performed to quantify the relative concentration of HSP-70 and HSP-90 in the above cell lysates.

2.19. Animal model

All animal procedures were performed in accordance with the Guidelines for Care and Use of Laboratory Animals of Sun Yat-sen University and approved by the Institutional Animal Care and Use Committee (IACUC) of Sun Yat-sen University (Approval number: SYSU-IACUC-2021-000398). Female BALB/c mice (18−22 g) were obtained from Guangdong Sijiajingda Biotechnology Co., Ltd. (Guangzhou, China). The animals were housed in a specific pathogen free (SPF) environment at a temperature of 22 ± 2 °C and were given free access to food and water.

2.20. In vivo biodistribution

The female BALB/c mice bearing 4T1 tumor were randomly divided into two groups ($n = 3$) and intravenously injected with free ICG and I-CaS@PP at an equivalent ICG concentration (10 mg/kg), respectively. The fluorescence images were captured at 2, 4, 6, 8, 12 and 24 h. Furthermore, at 24 h post-injection, the mice were sacrificed and the major organs (heart, liver, spleen, lung, and kidney) and tumors were excised for *ex vivo* imaging using the *in vivo* Imaging System (Berthold Technologies, NightOWL II LB983, Bad Wildbad, Germany). The fluorescence intensities of ICG in the main organs and tumors were quantified.

2.21. *In vivo photothermal imaging*

The mice bearing 4T1 tumor were administered with saline, free ICG, and I-CaS@PP at an equivalent ICG concentration (10 mg/kg) through tail vein injection. After injection for 12 h, the tumor sites in all groups were irradiated with 808 nm laser at 1.2 W/cm^2 for 5 min. The temperature variations in all groups were monitored by an IR thermal camera (TI100 Infrared Camera FLK-TI100 9HZ, FLUKE).

2.22. *In vivo anticancer effect*

The female BALB/c mice bearing 4T1 tumor were randomly divided into seven groups ($n = 5$): (1) saline as the control group; (2) saline + L to evaluate the influence of laser irradiation; (3) free ICG to assess the toxicity of free ICG; (4) ICG + L to evaluate the effect of free ICG under laser irradiation; (5) CaS@PP to assess H_2S-boosted Ca^{2+} accumulation in antitumor efficacy; (6) I-CaS@PP to determine the antitumor performance of combinational therapeutic agents including Ca^{2+} overload and H_2S release with no laser irradiation. (7) I-CaS@PP + L to determine the antitumor performance of combinational therapeutic agents, including Ca^{2+} overload, H_2S release and photothermal effect. When the tumor volume reached about 100 mm^3, the mice were injected with different formulations on days 1, 3 and 5 *via* tail vein at an equal ICG concentration of 10 mg/kg. At 12 h post-injection, the mice in saline + L, ICG + L and I-CaS@PP + L groups were anesthetized and received an 808 nm laser irradiation at 1.2 W/cm^2 for 5 min. The tumor volumes and body weights were recorded every two days. The tumor volume was calculated using Eq. (4):

$$\text{Tumor volume} = 0.5 \times (\text{Tumor width})^2 \times (\text{Tumor length}) \quad (4)$$

Fourteen days later, the mice were sacrificed and the tumors were excised, weighed and sliced for hematoxylin and eosin (HE) staining, Ki67 staining, TUNEL assay, DCFH-DA staining, HSP-70 and HSP-90 expression.

2.23. *Hemolysis assay*

The red blood cells were collected by centrifuging fresh mouse blood (2000 rpm, 10 min; Eppendorf) and washing with PBS three times. Then, 0.2 mL of 8% red blood cells (*v*/*v*) were mixed with 0.8 mL of deionized water, PBS, or I-CaS@PP solutions dissolved in PBS with various Ca^{2+} concentrations (1.25, 2.5, 5, 10, 20 and 40 μg/mL) at 37 °C for 2 h. Ultimately, all samples were centrifuged and the absorbance of the supernatants at 540 nm was detected using UV−Vis spectroscopy. The red blood cells in PBS and distilled water without nanoparticles were used as the negative and positive control, respectively.

2.24. *In vivo safety evaluation*

To evaluate systemic toxicity, blood samples of each mouse were collected and subjected to hematological analyses, including hepatic function tests aspartate transaminase (AST) and alanine transaminase (ALT), renal function markers blood urea nitrogen (BUN) and creatinine (CREA). Besides, the main organs (heart, liver, spleen, lung, and kidney) were also collected for hematoxylin−eosin (H&E) staining to inspect any histological change.

2.25. *Statistical analysis*

All results are presented as mean ± standard deviation (SD). Statistical analyses were performed using one-way ANOVA with SPSS 22.0 software, where $P < 0.05$ was considered as statistically significant. The differences were indicated as follows: $^*P < 0.05$, $^{**}P < 0.01$ and $^{***}P < 0.001$.

3. Results and discussion

3.1. *Synthesis and characterization*

To prepare I-CaS@PP, the CaS crystals were firstly synthesized using the high-temperature co-precipitation method as described in the previous study[25], which exhibited high dispersity, hexagon morphology with a uniform size of about 20 nm (Fig. 2A). The high-resolution TEM (HRTEM) image of CaS displayed clear lattice fringes with an observed *d* spacing of 0.203 nm (inset of Fig. 2A), which agreed well with the lattice spacing of the (220) plane of cubic CaS (JCPDS No. 008-0464) (Fig. 2D). Subsequently, both as-synthesized CaS crystals and indocyanine green (ICG) were stabilized by PLGA-PEG to obtain I-CaS@PP, which transformed into approximate spherical pellets and still remained distinct lattice structure (Fig. 2B and inset of Fig. 2B). Meanwhile, the significant changes in particulate size (changed from 20.62 to 164.76 nm) and zeta potential (changed from −56.49 ± 11.94 to −13.72 ± 0.73 mV) determined by the dynamic light scattering technique confirmed the successful construction of I-CaS@PP (Fig. 2C and Supporting Information Fig. S1). The loading amounts of CaS and ICG in I-CaS@PP were calculated to be 2.18% and 18.40%, respectively. The high stability of I-CaS@PP no matter in PBS or DMEM containing 10% FBS over 72 h confirmed the effective protective effect of PLGA-PEG on CaS against hydrolysis (Supporting Information Fig. S2). The characteristic diffraction peaks in X-ray diffraction (XRD) patterns evidenced the existence of cubic CaS in I-CaS@PP (Fig. 2D). The decreased peak intensity of I-CaS@PP after PEGylation was probably due to the cover of phospholipid bilayer on the surface of CaS. To further confirm the successful encapsulation of CaS and ICG in I-CaS@PP, high-angle annular dark-field scanning TEM (HAADF-STEM), energy-dispersive X-ray spectroscopy (EDX) and X-ray photoelectron spectroscopy (XPS) were conducted. As shown in Fig. 2E and Supporting Information Fig. S3, Ca, S, C, O and N elements were evenly dispersed in I-CaS@PP, indicating the successful preparation of I-CaS@PP. In addition, XPS of I-CaS@PP also confirmed the existence of Ca, S, C, O and N elements in I-CaS@PP (Supporting Information Fig. S4).

The structure and morphology of I-CaS@PP remained basically unchanged under physiological condition (pH = 7.4) for 12 h. In the meanwhile, I-CaS@PP were obviously ruptured after incubating in acidic buffer solution (pH = 6.5) for 2 h. Moreover, I-CaS@PP were remarkably degraded and completely degraded within 12 h in acidic buffer solution (pH = 5.5), confirming that I-CaS@PP not only ensured high biosafety in the blood circulation, but also contributed to the specific release of Ca^{2+} and H_2S in acidic tumor microenvironment for the treatment of malignant tumor (Fig. 2F). Subsequently, H_2S production efficiency from I-CaS@PP was evaluated by methylene blue method, which

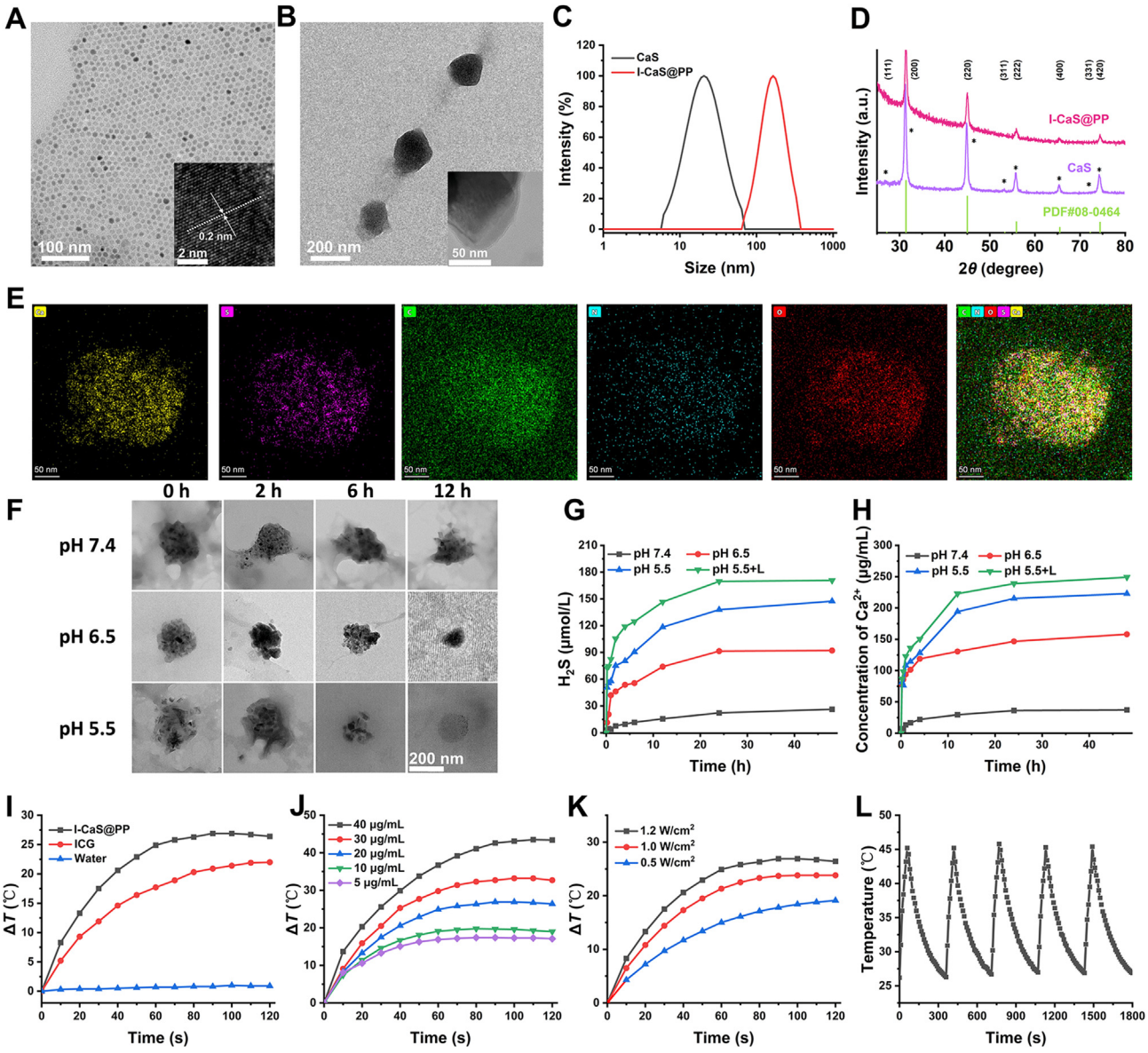

Figure 2 TEM images of (A) CaS and (B) I-CaS@PP. The insets in (A) and (B): HRTEM images of CaS and I-CaS@PP, respectively. (C) Hydrodynamic size and (D) X-ray diffraction (XRD) patterns of CaS and I-CaS@PP. (E) High-angle annular dark-field scanning TEM (HAADF-STEM) image and corresponding elemental mapping images of I-CaS@PP. (F) TEM images of I-CaS@PP after incubation in PBS buffer solutions with varied pH values (7.4, 6.5 or 5.5) at various time intervals. Scale bar = 200 nm. (G) Time-dependent H_2S release profile from I-CaS@PP at different pH values (7.4, 6.5 or 5.5) with or without 808 nm laser irradiation (1.2 W/cm^2). (H) Specific Ca^{2+} release from I-CaS@PP at different pH values with or without 808 nm laser irradiation (1.2 W/cm^2). (I) Temperature elevation curves of pure water, ICG, and I-CaS@PP under 808 nm laser irradiation (1.2 W/cm^2) for 2 min. (J) Photothermal heating curves of I-CaS@PP at different concentrations under 808 nm laser irradiation (1.2 W/cm^2) for 2 min. (K) Photothermal heating curves of I-CaS@PP under various power intensities. (L) Photothermal conversion stability of I-CaS@PP aqueous solution for five laser on/off cycles with an 808 nm laser irradiation (1.2 W/cm^2).

revealed pH and concentration dependent behaviors (Fig. 2G and Supporting Information Fig. S5). The generated amount of H_2S was kept relatively stable in neutral solution for 48 h incubation while significantly elevated after incubating in acidic solution (pH = 6.5) for only 1 h. Moreover, the concentration of released H_2S could reach as high as about 150 μmol/L when pH of the solution further reduced to 5.5 at 48 h incubation. The higher the concentration of I-CaS@PP, the more H_2S was produced (Fig. S5). More interestingly, laser irradiation would speed up H_2S generation, which might be because ICG-induced photothermal effect under laser exposure accelerated the disintegration of I-CaS@PP (Fig. 2G)[29]. Similarly, the release of Ca^{2+} showed the same trend as the generation of H_2S, which was also pH and time dependent (Fig. 2H). Moreover, laser irradiation would also prominently enhance the release of Ca^{2+}. Due to the acidic tumor microenvironment compared to normal tissue, I-CaS@PP were capable of achieving tumor-specific H_2S and Ca^{2+} release.

The photothermal conversion efficiency of I-CaS@PP was further investigated by monitoring the temperature change (ΔT) under 808 nm laser irradiation using an infrared thermal

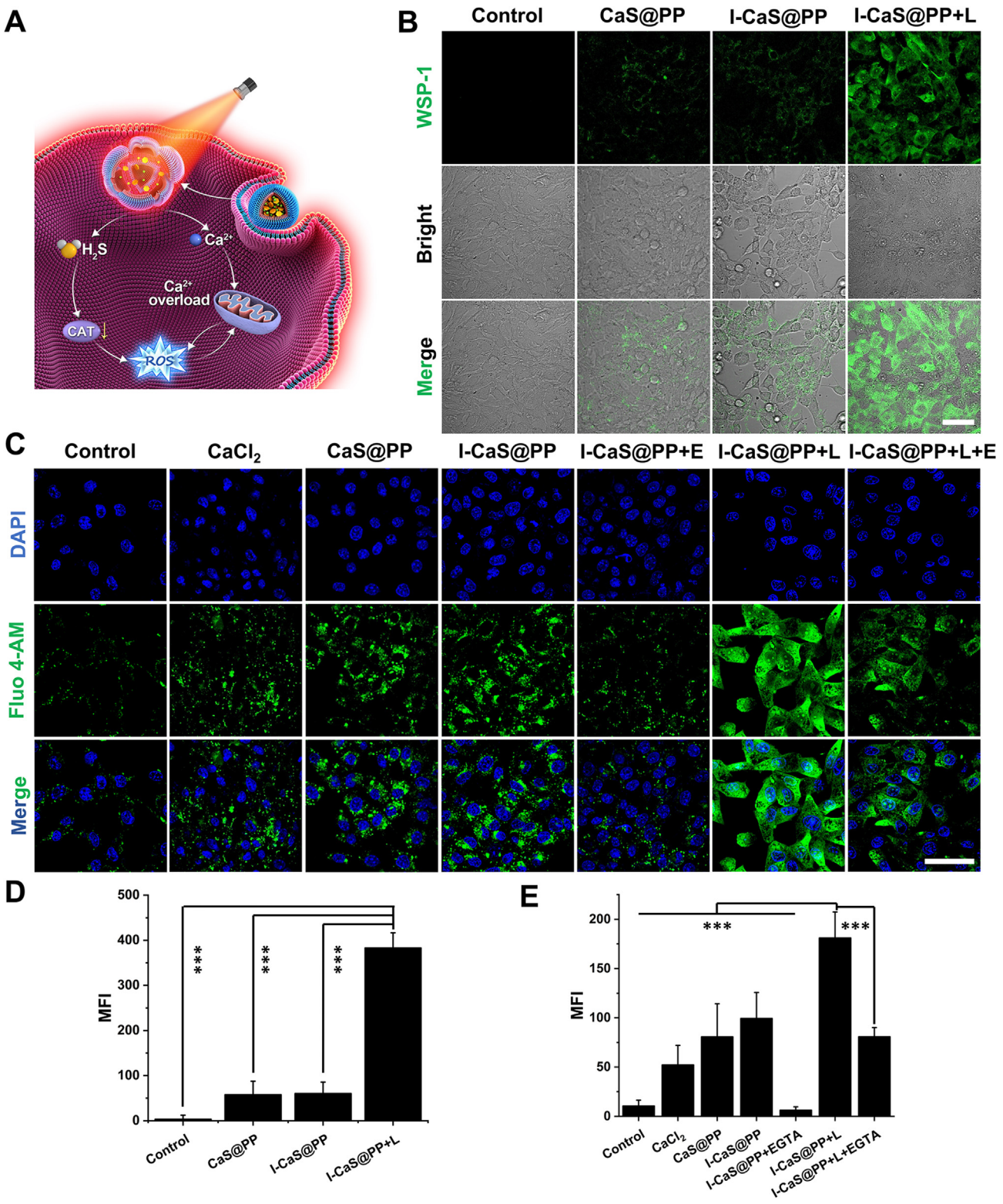

Figure 3 (A) Schematic illustration of synergistic therapeutic mechanism of I-CaS@PP. (B) CLSM images and (D) corresponding mean fluorescence intensity (MFI) of intracellular H_2S level after different treatments for 6 h. Scale bar = 50 μm. (C) CLSM images and (E) corresponding MFI of intracellular Ca^{2+} concentration after various treatments for 6 h. Scale bar = 50 μm. Data are presented as mean ± SD ($n = 3$). ***$P < 0.001$. L means NIR laser irradiation, E means EGTA.

imaging camera. In contrast to the almost constant temperature of pure water under irradiation (1.2 W/cm^2, 2 min), ΔT of free ICG and I-CaS@PP increased by about 22 and 26.4 °C, respectively (Fig. 2I). The temperature rise of I-CaS@PP was higher than that of free ICG indicating the elevated stability of ICG after being encapsulated into I-CaS@PP. In addition, the

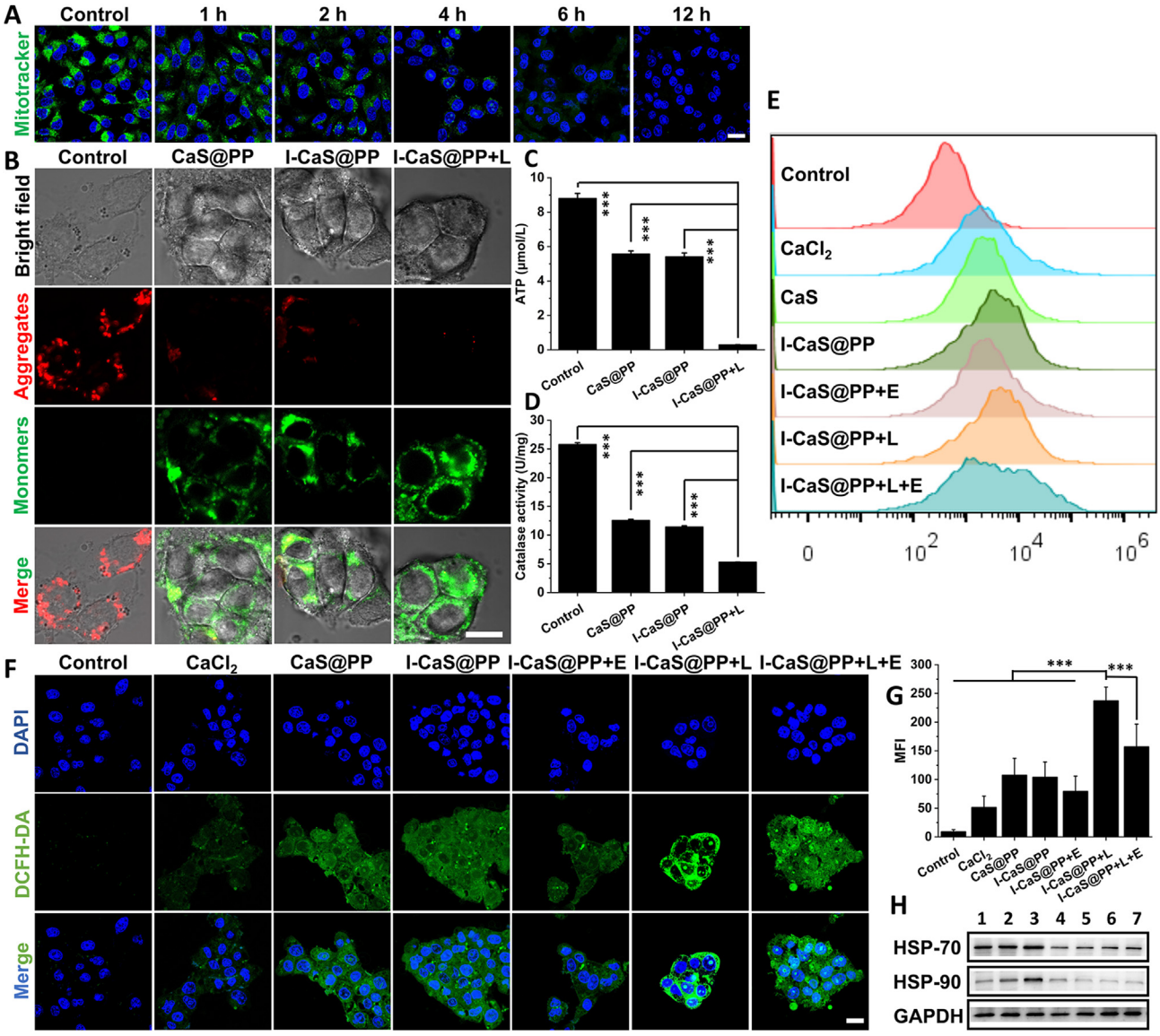

Figure 4 (A) CLSM images of cellular mitochondrial state (Mitotracker) and nuclei (Hoechst) in 4T1 cells at different time points. Scale bar = 20 μm. (B) CLSM images of the mitochondrial membrane potential in 4T1 cells after different treatments indicated by JC-1 monomer (green) and aggregate (red). Scale bar = 10 μm. (C) Intracellular ATP content analysis. (D) Intracellular catalase activity analysis. Intracellular ROS generation in 4T1 cells after different treatments determined by (E) flow cytometry and (F) CLSM images. Scale bar = 20 μm. (G) Quantitative MFI values of intracellular ROS in 4T1 cells in different groups. Data are presented as the mean ± SD (n = 3). (H) Western blot assay for detecting the expressions of HSP-70 and HSP-90 in 4T1 cells after various treatments. 1: Control; 2: Control +40 °C; 3: $CaCl_2$ + 40 °C; 4: CaS@PP; 5: I-CaS@PP; 6: I-CaS@PP + L; 7: I-CaS@PP + L + E. Data are presented as mean ± SD (n = 3). ***$P < 0.001$. L means NIR laser irradiation, E means EGTA.

photothermal conversion capability of I-CaS@PP was concentration and power dependent (Fig. 2J and K). The higher concentration of I-CaS@PP or the stronger power density of laser, the more thermal energy was obtained. The photothermal conversion efficiency (η) of I-CaS@PP was calculated to be 12.88% at 808 nm (Supporting Information Fig. S6). Furthermore, after treatment with five cycles of on/off laser irradiation, the photothermal conversion effect was notably declined in free ICG but kept unchanged in I-CaS@PP, further confirming the superior protective performance of PLGA-PEG on ICG and excellent photothermal conversion stability of I-CaS@PP (Fig. 2L and Supporting Information Fig. S7).

3.2. *In vitro antitumor effect and underlying mechanism*

To further explore the antitumor effect, cellular uptake profile of I-CaS@PP against 4T1 cells was assessed by confocal laser scanning microscopy (CLSM) and flow cytometry. As shown in Supporting Information Fig. S8A, the red fluorescence signal of ICG in I-CaS@PP intensified with the prolonged incubation time, illustrating that I-CaS@PP could be efficiently internalized by 4T1 cells, consistent with quantitative flow cytometric analysis (Fig. S8B).

Subsequently, in order to investigate the release of H_2S in tumor cells (Fig. 3A), a H_2S-specific fluorescence probe WSP-1

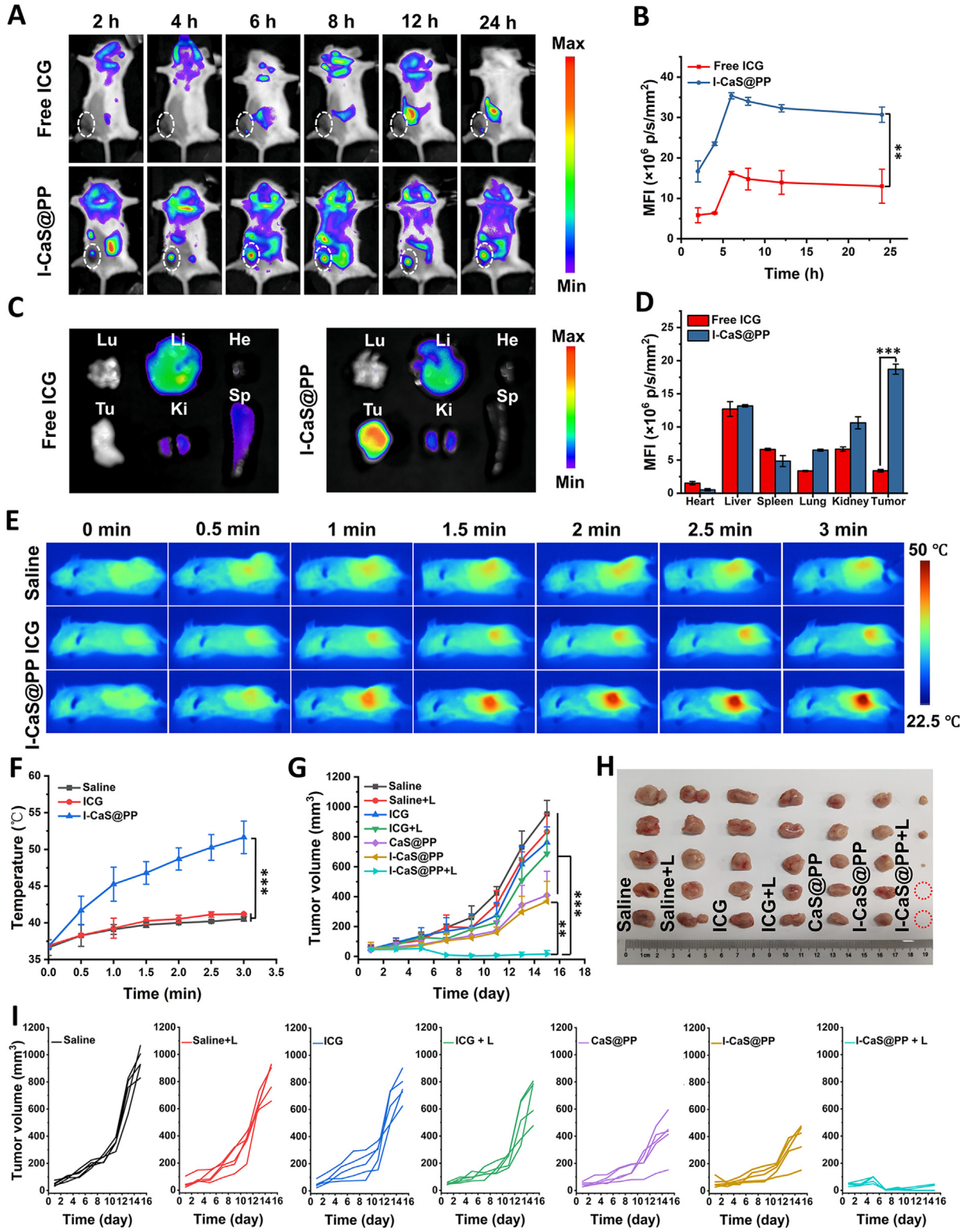

Figure 5 (A) *In vivo* fluorescence images of 4T1 tumor-bearing mice after intravenous injection of free ICG and I-CaS@PP at different time points and (B) corresponding MFI values in the tumor site. Data are presented as mean ± SD ($n = 3$). $^{**}P < 0.01$. (C) *Ex vivo* fluorescence images and (D) corresponding MFI values of major organs and tumor tissue harvested at 24 h postinjection. He: heart, Li: liver, Sp: spleen, Lu: lung, Ki: kidney, and Tu: tumor. Data are presented as mean ± SD ($n = 3$). $^{***}P < 0.001$. (E) *In vivo* IR thermal images of 4T1 tumor-bearing mice in different groups under 808 nm laser irradiation (1.2 W/cm^2) taken at different time intervals. (F) Corresponding temperature change in the tumor site with different treatments during laser irradiation. Data are presented as mean ± SD ($n = 3$). $^{***}P < 0.001$. (G) Tumor growth curves after intravenous injection of saline, saline + L, ICG, ICG + L, CaS@PP, I-CaS@PP and I-CaS@PP + L. Data are presented as mean ± SD ($n = 5$). $^{**}P < 0.01$, $^{***}P < 0.001$. (H) Tumor tissues excised from euthanized 4T1 tumor-bearing mice after different treatments. (I) Individual tumor growth curves of mice in different groups. L means NIR laser irradiation.

was employed. As shown in Fig. 3B and D, compared to the cells in the control group, the green fluorescence was slightly elevated in cells treated with CaS@PP and I-CaS@PP, verifying the effective internalization by 4T1 cells and the definite hydrolysis in acidic endosomes. Impressively, H_2S green fluorescence could be prominently enhanced in cells receiving I-CaS@PP + L treatment, stating that the thermal energy resulting from photothermal conversion reaction would promote the disintegration of I-CaS@PP and the production of H_2S. Moreover, it was worth noting that with the generation of H_2S, abundant Ca^{2+} was speculated to be released from I-CaS@PP. Studies have shown that H_2S can facilitate membrane potential depolarization and calcium influx by opening calcium permeable channels[30]. Therefore, intracellular Ca^{2+} content was next examined using a Fluo-4 AM probe, which emitted green fluorescence in the presence of free Ca^{2+} (Fig. 3C). Similar to intracellular H_2S level, the cells treated with I-CaS@PP + L exhibited the highest Ca^{2+} content. To confirm the promoting effect of H_2S gas on intracellular Ca^{2+} level, 4T1 cells were co-incubated with EGTA (a specific calcium ion chelator) and I-CaS@PP. As indicated in Fig. 3C and E, the green fluorescence was fairly weak in I-CaS@PP + EGTA group, which was comparable to that in the control group, illustrating the highly efficient Ca^{2+} deprivation after EGTA treatment. However, the green fluorescence was still strong in cells treated with I-CaS@PP + L + EGTA, further demonstrating the important role of thermal energy in promoting H_2S production and subsequent H_2S-boosted Ca^{2+} elevation.

Inspired by the excellent capability of I-CaS@PP to produce H_2S and Ca^{2+} in acidic tumor microenvironment, its *in vitro* antitumor efficacy against 4T1 tumor cells was evaluated. The results showed that the survival rates of 4T1 tumor cells notably reduced with the increase of CaS@PP and I-CaS@PP concentrations, suggesting that the generated H_2S and Ca^{2+} would upregulate oxidative stress and induce tumor cell death (Supporting Information Fig. S9A). Moreover, the tumor-killing effect of I-CaS@PP would be further intensified with exposure to laser irradiation due to the outstanding photothermal effect of ICG. Live/dead cell double staining using calcein-acetoxymethyl ester (calcein-AM, green fluorescence) and propidium iodide (PI, red fluorescence) Kit also confirmed the strong tumor-damaging performance of I-CaS@PP + L (Fig. S9B). The cell viabilities determined by flow cytometry assay displayed that the cell mortality rate in I-CaS@PP + L group was extremely high, which could reach early apoptosis of 2.06%, late apoptosis of 32.3%, and necrosis of 48.3% (Fig. S9C).

3.3. *Mitochondrial damage and photothermal therapy mechanism*

Mitochondria are important organelles that produce energy and regulate cell apoptosis, playing a variety of functions in physiological and pathological scenarios. It is well known that most of Ca^{2+} in cells are stored in the mitochondria and endoplasmic reticulum, and its abnormal retention can induce intracellular oxidative stress[31–33]. Therefore, the influence of I-CaS@PP on mitochondrial homeostasis was initially evaluated by observing the mitochondrial damage using MitoTracker® Green FM, a mitochondrion-specific probe that could label the active mitochondria. Relative to the control group, the green fluorescence in I-CaS@PP treated cells weakened gradually over time and disappeared completely at 12 h, illustrating the structural damage of mitochondria caused by I-CaS@PP, which might be attributed to the massive release of Ca^{2+} and H_2S in the acidic tumor microenvironment (Fig. 4A). Additionally, the mitochondrial membrane potential change ($\Delta\psi_m$) was next measured through JC-1 staining that formed *J*-aggregates emitting red fluorescence in normal mitochondrial membranes but presented green fluorescent monomers in depolarized mitochondrial membrane. As presented in Fig. 4B, the strong green fluorescence signals were observed in 4T1 cells after incubation with CaS@PP, I-CaS@PP and I-CaS@PP + L, indicating the significant decline of mitochondrial membrane potential and severe mitochondrial damage. Notably, the cells in I-CaS@PP + L group showed the most destructive effect on mitochondrial integrity.

The mitochondrial dysfunction demonstrated above may be attributed to disruption of the mitochondrial electronic respiratory chain in the inner mitochondria membrane that establishes $\Delta\psi_m$ for ATP synthesis[33–35]. As shown in Fig. 4C, ATP content decreased substantially in cells after treated with CaS@PP and I-CaS@PP, which dropped to about only 0.3 μmol/L after laser irradiation, revealing the remarkable cut-off of energy supply. In the meanwhile, the effect of H_2S gas on CAT activity of 4T1 cells was further explored by CAT assay kit according to its protocol (Fig. 4D). The results show that the activity of intracellular CAT was effectively suppressed after CaS@PP and I-CaS@PP treatments due to the generated H_2S, which would be further inhibited with exposure to laser irradiation, proving that ICG-mediated thermal energy stimulated H_2S production. It is well known that CAT is an antioxidant enzyme overexpressed in tumor cells that catalyzes H_2O_2 into water and oxygen, which influences cancer progression and strengthens resistance to various therapies[36–42]. Therefore, the decrease of CAT activity affected by H_2S may contribute to inhibit the decomposition of harmful substance H_2O_2 and elevate intracellular oxidative stress[16]. Inspiringly, the intracellular ROS level was detected by cell-permeant 2′,7′-dichlorofluorescein diacetate (DCFH-DA) fluorescent probe *via* CLSM images and flow cytometry (Fig. 4E–G). Compared to the control group, the green fluorescence was enhanced in cells treated with $CaCl_2$ owing to the abnormal retention of Ca^{2+} in cells. Furthermore, the stronger green fluorescence in CaS@PP and I-CaS@PP groups than that in $CaCl_2$ group indicated the upregulated oxidative stress derived from H_2S-suppressed CAT activity. The strongest green fluorescence in I-CaS@PP + L group and slightly declined fluorescence intensity in I-CaS@PP + EGTA and I-CaS@PP + L + EGTA groups suggested the highest intracellular ROS level after I-CaS@PP + L treatment, confirming the superior therapeutic effect on tumor cells.

Generally, the heat endurance of tumors is mainly attributed to HSPs, whose expression depends on the energy supply of ATP. Here, I-CaS@PP + L induced mitochondrial dysfunction and ATP decline would definitely downregulate the expression of HSPs, which was ultimately conducive to enhancing the efficacy of PTT. Thus, two main HSPs, HSP-70 and HSP-90, were detected by western blotting (WB) assay. As shown in Fig. 4H and Supporting Information Fig. S10, compared with control group, control +40 °C and $CaCl_2$ + 40 °C groups exhibited much more expression of HSPs owing to high temperature processing. However, much fewer HSPs expressions were detected in CaS@PP, I-CaS@PP, I-CaS@PP + L and I-CaS@PP + L + EGTA groups, validating that CaS-mediated inhibition of ATP synthesis significantly cut off the energy supply of HSPs expression. Collectively, these results suggest that H_2S-boosted Ca^{2+} overload could be effective to augment PTT by downregulating the expression of heat-resistant proteins.

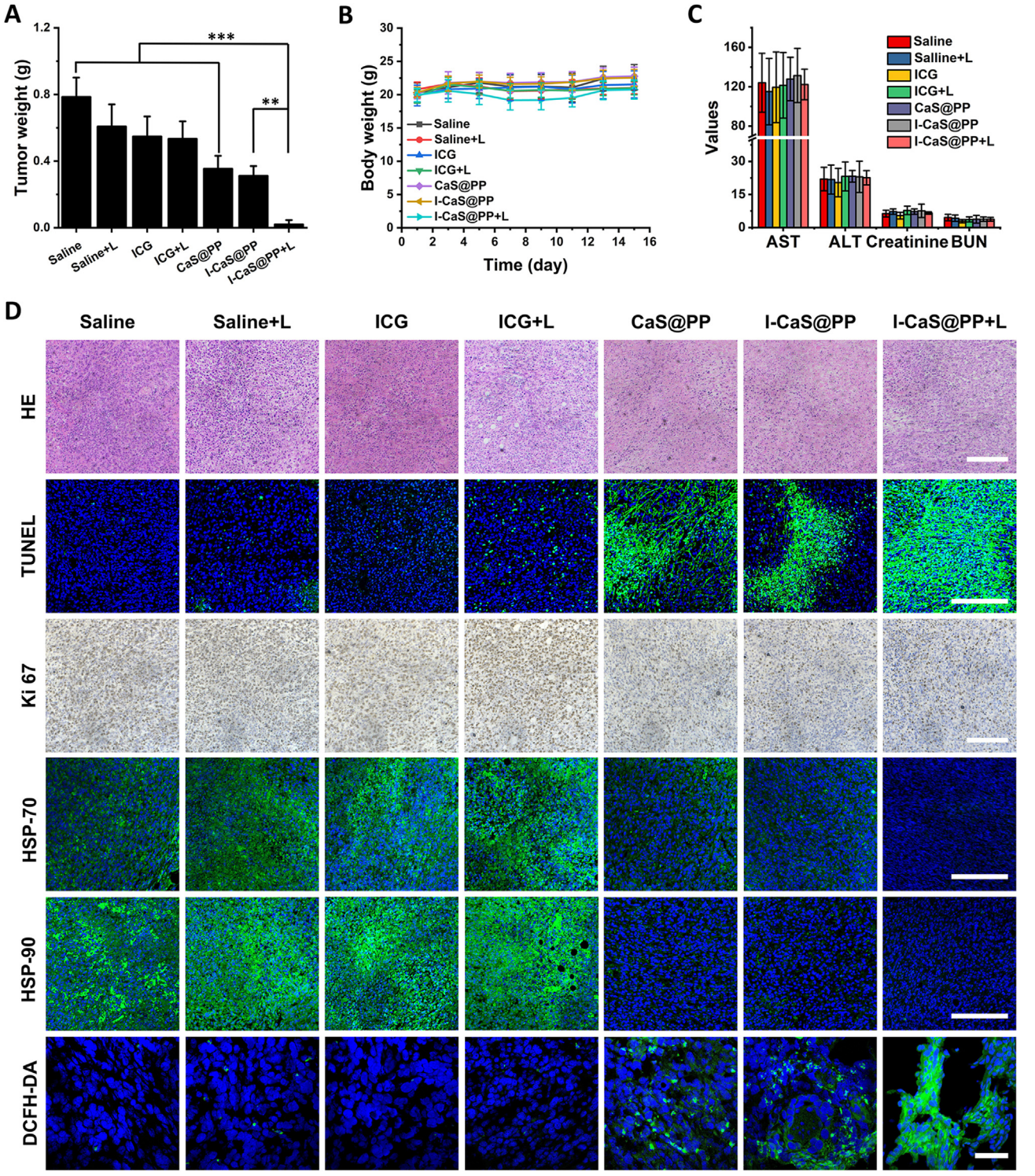

Figure 6 (A) The tumor weight removed from the 4T1 tumor-bearing mice in different groups at the end of the experiment. (B) Body weight changes of the tumor-bearing mice during different treatments. (C) Hepatic and renal function indicators of mice bearing 4T1 tumor xenografts at the end of treatment. (D) HE staining, TUNEL immunofluorescence staining, Ki-67 antibody staining, immunofluorescence images of the expressions of HSP-70 and HSP-90, and DCFH-DA staining images in tumor tissues collected from 4T1-bearing mice with different treatments. Scale bar are 200 μm or 50 μm (DCFH-DA). Data are presented as mean ± SD ($n = 5$). $^{**}P < 0.01$, $^{***}P < 0.001$. L means NIR laser irradiation.

3.4. In vivo biodistribution and therapeutic efficacy

The *in vivo* biodistribution of I-CaS@PP was investigated by intravenous administration of I-CaS@PP into 4T1 tumor-bearing BALB/c mice and tracking the fluorescence of ICG at different time intervals. As shown in Fig. 5A and B, compared to free ICG group, much stronger fluorescent signals clearly appeared in the tumor site in I-CaS@PP group. Moreover, the fluorescence

intensity in the tumor region reached its maximum at 6 h post injection and still remained high until 24 h, stating the effective accumulation and retention of I-CaS@PP in the tumor tissue. At 24 h post injection, all mice were sacrificed and the major organs and tumors were excised for *ex vivo* fluorescence imaging, which further confirmed that I-CaS@PP were mainly distributed in the tumor tissue rather than other major organs (Fig. 5C and D).

Since I-CaS@PP exhibited excellent photothermal conversion effect and stability *in vitro*, its photothermal performance *in vivo* was subsequently assessed on 4T1 tumor-bearing BALB/c mice using an infrared thermal imaging camera (Fig. 5E and F). It was found that the tumor surface temperature in free ICG + L group was comparable to that in control group, which was attributed to the minimal enrichment of ICG in tumor tissue. However, the temperature of the tumor tissue in I-CaS@PP + L group increased significantly, reaching about 51.63 °C, which was sufficient to ablate tumor cells.

Inspired by the satisfactory tumor inhibition efficacy *in vitro* and excellent biodistribution *in vivo*, we studied the therapeutic efficacy of I-CaS@PP + L *in vivo*. The 4T1 tumor-bearing mice were randomly divided into seven groups and intravenously injected into various formulas: saline, saline + L, ICG, ICG + L, CaS@PP, I-CaS@PP and I-CaS@PP + L group. As exhibited in Fig. 5G–I and Fig. 6A, the tumors grew rapidly in saline, saline + L, ICG, and ICG + L groups, proving that laser irradiation alone had scarcely any tumor suppression effect and the accumulation of ICG in tumor tissue was low. The mice treated with CaS@PP and I-CaS@PP exhibited certain inhibition on tumor growth, owing to the abundant H_2S and Ca^{2+} generation in acidic tumor microenvironment. Impressively, the tumors in mice treated with I-CaS@PP + L were almost eliminated within 14 days, which demonstrated the great potential of I-CaS@PP as an effective therapeutic agent for combating malignant tumors under laser irradiation.

The antitumor effect of I-CaS@PP + L was further confirmed by H&E staining and terminal deoxynucleotidyl transferase dUTP nick-end labeling (TUNEL) immunofluorescence staining of tumor slices, which showed the most serious tumor cell apoptosis and necrosis in I-CaS@PP + L group (Fig. 6D). Moreover, Ki-67 antibody staining presenting proliferative activities further demonstrated I-CaS@PP + L had the strongest suppression effect on the tumor cell proliferation. In the meantime, the possible anti-proliferative mechanism was explored by the immunofluorescence assays. On the one hand, compared to saline, saline + L, ICG and ICG + L groups, the expressions of HSPs including HSP-70 and HSP-90 were much less in CaS@PP, I-CaS@PP, and I-CaS@PP + L groups, which contributed to promoting the efficacy of PTT (Fig. 6D). On the other hand, the significantly suppressed tumor growth in I-CaS@PP + L could be attributed to the strongest ROS generation in tumor tissue after I-CaS@PP + L treatment (Fig. 6D).

In addition, the body weights were measured to assess *in vivo* systematic toxicity of different formulas after intravenous administration. Fig. 6B illustrates that all the groups showed no distinct difference in body weights. Further, the low hemolytic effect of I-CaS@PP at the Ca^{2+} concentration of 40 μg/mL indicated the good hemocompatibility of I-CaS@PP (Supporting Information Fig. S11). Hematological parameters such as serum aspartate transaminase (AST), alanine transaminase (ALT), creatinine and blood urea nitrogen (BUN) revealed normal liver and kidney function in all treatment groups (Fig. 6C). Moreover, there was no difference in H&E-stained histopathological images of major organs between the control and all treatment groups (Supporting Information Fig. S12). All these results indicate that I-CaS@PP + L possessed the powerful antitumor activity with high biosafety.

4. Conclusions

We have successfully developed CaS-based nanomodulators (I-CaS@PP) for H_2S-boosted Ca^{2+}-involved tumor-specific therapy with powerful therapeutic effect and excellent pH-responsive biodegradability. The released H_2S could not only suppress CAT activity, but also promote calcium influx, thereby synergistically damaging mitochondria and amplifying oxidative stress. The dysfunction of mitochondria diminished intracellular energy supply and downregulated ATP-dependent expression of HSPs, which remarkably reversed tumor heat resistance and enhanced ICG-induced photothermal performance. Both *in vitro* and *in vivo* results demonstrated that I-CaS@PP could serve as a promising synergistic cascade platform to achieve efficient antitumor efficacy by increasing intracellular oxidative stress and restraining tumor heat resistance.

Acknowledgments

The authors gratefully acknowledge the support of this research by the National Natural Science Foundation of China (31922042, 81971737, 32171313), Guangdong Basic and Applied Basic Research Foundation (2020B1515020017, China), Shenzhen Science and Technology Program (RCYX20210706092104033, China), Science and Technology Innovation Committee of Shenzhen Municipality (JCYJ20190807152601651, China), Guangdong Special Support Program (2019TQ05Y224, China), the Fundamental Research Funds for the Central Universities (2021-RC310-005, 2020-RC320-002 and 2019PT320028, China), and Chinese Academy of Medical Sciences Innovation Fund for Medical Sciences (2021-I2M-1-058, China).

Author contributions

Chuchu Lin and Meiying Wu conceived and designed the research. Chuchu Lin carried out the experiments and performed data analysis. Chenyi Huang, Zhaoqing Shi, Meitong Ou and Shengjie Sun participated part of the experiments. Mian Yu, Lin Mei and Feng Lv provided some suggestions to the research designs. Ting Chen and Yunfei Yi provided some supports of cell culture. Meiying Wu, Lin Mei and Xiaoyuan Ji supervised the research. Chuchu Lin, Meiying Wu and Lin Mei wrote the manuscript.

Conflicts of interest

The authors declare no conflict of interest.

Appendix A. Supporting information

Supporting data to this article can be found online at https://doi.org/10.1016/j.apsb.2022.08.008.

References

1. Szabo C. Gasotransmitters in cancer: from pathophysiology to experimental therapy. *Nat Rev Drug Discov* 2016;**15**:185–203.

2. Wang R. Physiological implications of hydrogen sulfide: a whiff exploration that blossomed. *Physiol Rev* 2012;**92**:791−896.
3. Wallace JL, Wang R. Hydrogen sulfide-based therapeutics: exploiting a unique but ubiquitous gasotransmitter. *Nat Rev Drug Discov* 2015; **14**:329−45.
4. Paul BD, Snyder SH. H_2S signalling through protein sulfhydration and beyond. *Nat Rev Mol Cell Biol* 2012;**13**:499−507.
5. Ren H, Yong JH, Yang QQ, Yang Z, Liu ZY, Xu Y, et al. Self-assembled FeS-based cascade bioreactor with enhanced tumor penetration and synergistic treatments to trigger robust cancer immunotherapy. *Acta Pharm Sin B* 2021;**11**:3244−61.
6. He JT, Li HQ, Yang L, Mao CY. Role of hydrogen sulfide in cognitive deficits: evidences and mechanisms. *Eur J Pharmacol* 2019;**849**: 146−53.
7. Li Z, Polhemus DJ, Lefer DJ. Evolution of hydrogen sulfide therapeutics to treat cardiovascular disease. *Circ Res* 2018;**123**: 590−600.
8. Wallace JL, Vaughan D, Dicay M, MacNaughton WK, de Nucci G. Hydrogen sulfide-releasing therapeutics: translation to the clinic. *Antioxid Redox Signaling* 2018;**28**:1533−40.
9. Predmore BL, Lefer DJ, Gojon G. Hydrogen sulfide in biochemistry and medicine. *Antioxid Redox Signaling* 2012;**17**:119−40.
10. Liu J, Ren L, Li S, Li W, Zheng X, Yang Y, et al. The biology, function, and applications of exosomes in cancer. *Acta Pharm Sin B* 2021;**11**:2783−97.
11. Li QQ, Shi ZQ, Zhang F, Zeng WW, Zhu DW, Mei L. Symphony of nanomaterials and immunotherapy based on the cancer−immunity cycle. *Acta Pharm Sin B* 2022;**12**:107−34.
12. Panagaki T, Randi EB, Augsburger F, Szabo C. Overproduction of H_2S, generated by CBS, inhibits mitochondrial complex IV and suppresses oxidative phosphorylation in down syndrome. *Proc Natl Acad Sci U S A* 2019;**116**:18769−71.
13. Paul BD, Snyder SH, Kashfi K. Effects of hydrogen sulfide on mitochondrial function and cellular bioenergetics. *Redox Biol* 2021;**38**: 101772.
14. Ngowi EE, Afzal A, Sarfraz M, Khattak S, Zaman SU, Khan NH, et al. Role of hydrogen sulfide donors in cancer development and progression. *Int J Biol Sci* 2021;**17**:73−88.
15. Li L, Rose P, Moore PK. Hydrogen sulfide and cell signaling. *Annu Rev Pharmacol Toxicol* 2011;**51**:169−87.
16. Xie CK, Cen D, Ren ZH, Wang YF, Wu YJ, Li X, et al. FeS@BSA nanoclusters to enable H_2S -amplified ROS-based therapy with mri guidance. *Adv Sci* 2020;**7**:1903512.
17. Yang ZB, Luo Y, Hu YA, Liang KC, He G, Chen Q, et al. Photothermo-promoted nanocatalysis combined with H_2S-mediated respiration inhibition for efficient cancer therapy. *Adv Funct Mater* 2021; **31**:2007991.
18. Sun QQ, Wang Z, Liu B, He F, Gai SL, Yang PP, et al. Recent advances on endogenous/exogenous stimuli-triggered nanoplatforms for enhanced chemodynamic therapy. *Coord Chem Rev* 2022; **451**:214267.
19. Munaron L, Avanzato D, Moccia F, Mancardi D. Hydrogen sulfide as a regulator of calcium channels. *Cell Calcium* 2013;**53**:77−84.
20. Chu X, Jiang XW, Liu YY, Zhai SJ, Jiang YQ, Chen Y, et al. Nitric oxide modulating calcium store for Ca^{2+}-initiated cancer therapy. *Adv Funct Mater* 2021;**31**:2008507.
21. Zhang M, Song RX, Liu YY, Yi ZG, Meng XF, Zhang JW, et al. Calcium-overload-mediated tumor therapy by calcium peroxide nanoparticles. *Chem* 2019;**5**:2171−82.
22. Chen QW, Liu XH, Fan JX, Peng SY, Wang JW, Wang XN, et al. Self-mineralized photothermal bacteria hybridizing with mitochondria-targeted metal-organic frameworks for augmenting photothermal tumor therapy. *Adv Funct Mater* 2020;**30**:1909806.
23. Li XC, Peris D, Hittinger CT, Sia EA, Fay JC. Mitochondria-encoded genes contribute to evolution of heat and cold tolerance in yeast. *Sci Adv* 2019;**5**:eaav 1848.
24. Lin CC, Hao HS, Mei L, Wu MY. Metal-free two-dimensional nanomaterial-mediated photothermal tumor therapy. *Smart Mater Med* 2020;**1**:150−67.
25. Zhang MR, Zheng W, Liu Y, Huang P, Gong ZL, Wei JJ, et al. A new class of blue-led-excitable NIR-II luminescent nanoprobes based on lanthanide-doped cas nanoparticles. *Angew Chem Int Ed* 2019;**58**: 9556−60.
26. Roper DK, Ahn W, Hoepfner M. Microscale heat transfer transduced by surface plasmon resonant gold nanoparticles. *J Phys Chem C* 2007; **111**:3636−41.
27. Ren WZ, Yan Y, Zeng LY, Shi ZZ, Gong A, Schaaf P, et al. A near infrared light triggered hydrogenated black TiO_2 for cancer photothermal therapy. *Adv Healthcare Mater* 2015;**4**:1526−36.
28. Zeng WW, Wu XX, Chen T, Sun SJ, Shi ZF, Liu J, et al. Renal-clearable ultrasmall polypyrrole nanoparticles with size-regulated property for second near-infrared light-mediated photothermal therapy. *Adv Funct Mater* 2021;**31**:2008362.
29. Xu LH, Tong GH, Song QL, Zhu CY, Zhang HL, Shi JJ, et al. Enhanced intracellular Ca^{2+} nanogenerator for tumor-specific synergistic therapy *via* disruption of mitochondrial Ca^{2+} homeostasis and photothermal therapy. *ACS Nano* 2018;**12**:6806−18.
30. Bauer CC, Boyle JP, Porter KE, Peers C. Modulation of Ca^{2+} signalling in human vascular endothelial cells by hydrogen sulfide. *Atherosclerosis* 2010;**209**:374−80.
31. Orrenius S, Zhivotovsky B, Nicotera P. Regulation of cell death: the calcium−apoptosis link. *Nat Rev Mol Cell Biol* 2003;**4**:552−65.
32. Tseng YC, Yang A, Huang L. How does the cell overcome LCP nanoparticle-induced calcium toxicity?. *Mol Pharm* 2013;**10**:4391−5.
33. Dong ZL, Feng LZ, Hao Y, Li QG, Chen MC, Yang ZJ, et al. Synthesis of $CaCO_3$-based nanomedicine for enhanced sonodynamic therapy *via* amplification of tumor oxidative stress. *Chem* 2020;**6**:1391−407.
34. Ou M, Lin C, Wang Y, Lu Y, Wang W, Li Z, et al. Heterojunction engineered bioactive chlorella for cascade promoted cancer therapy. *J Control Release* 2022;**345**:755−69.
35. Zorova LD, Popkov VA, Plotnikov EY, Silachev DN, Pevzner IB, Jankauskas SS, et al. Mitochondrial membrane potential. *Anal Biochem* 2018;**552**:50−9.
36. Sies H, Jones DP. Reactive oxygen species (ROS) as pleiotropic physiological signalling agents. *Nat Rev Mol Cell Biol* 2020;**21**: 363−83.
37. Kim EK, Jang M, Song MJ, Kim D, Kim Y, Jang HH. Redox-mediated mechanism of chemoresistance in cancer cells. *Antioxidants* 2019;**8**: 471−88.
38. Yu M, Yu J, Yi Y, Chen T, Yu L, Zeng W, et al. Oxidative stress-amplified nanomedicine for intensified ferroptosis-apoptosis combined tumor therapy. *J Control Release* 2022;**347**:104−14.
39. Lei T, Yang Z, Xia X, Chen Y, Yang X, Xie R, et al. A nanocleaner specifically penetrates the blood−brain barrier at lesions to clean toxic proteins and regulate inflammation in Alzheimer's disease. *Acta Pharm Sin B* 2021;**11**:4032−44.
40. Xu J, Du W, Zhao Y, Lim K, Lu L, Zhang C, et al. Mitochondria targeting drugs for neurodegenerative diseases-Design, mechanism and application. *Acta Pharm Sin B* 2022;**12**:2778−89.
41. He Y, Zheng Z, Liu C, Li W, Zhao L, Nie G, et al. Inhibiting DNA methylation alleviates cisplatin-induced hearing loss by decreasing oxidative stress-induced mitochondria-dependent apoptosis *via* the LRP1-PI3K/AKT pathway. *Acta Pharm Sin B* 2022;**12**:1305−21.
42. Li Z, Yang Y, Wei H, Shan X, Wang X, Ou M, et al. Charge-reversal biodegradable MSNs for tumor synergetic chemo/photothermal and visualized therapy. *J Control Release* 2021;**338**:719−30.